

Minute-Scale Photonic Quantum Memory

You-Cai Lv,^{1, 2, 3, 4} Yu-Jia Zhu,^{1, 2, 3, 4} Zong-Quan Zhou,^{1, 2, 3, 4, *} Chuan-Feng Li,^{1, 2, 3, 4} and Guang-Can Guo^{1, 2, 3, 4}

¹*Laboratory of Quantum Information,
University of Science and Technology of China, Hefei, 230026, China*

²*Anhui Province Key Laboratory of Quantum Network,
University of Science and Technology of China, Hefei 230026, China*

³*CAS Center For Excellence in Quantum Information and Quantum Physics,
University of Science and Technology of China, Hefei, 230026, China*

⁴*Hefei National Laboratory, University of Science and Technology of China, Hefei 230088, China*

(Dated: December 2, 2025)

Long-lived storage of single photons is a fundamental requirement for enabling quantum communication and foundational tests of quantum physics over extended distances. While the implementation of a global-scale quantum network requires quantum storage times on the order of seconds to minutes, existing photonic quantum memories have so far been limited to subsecond lifetimes. Although $^{151}\text{Eu}^{3+}:\text{Y}_2\text{SiO}_5$ crystals exhibit substantially extended spin coherence times at the ‘magic’ magnetic field, the concomitant weak optical absorption has until now prevented single-photon storage. Here, we overcome this challenge by integrating a noiseless photon echo protocol—which makes full use of the crystal’s natural absorption for photonic storage—with a universally robust dynamical decoupling sequence incorporating adiabatic pulses to efficiently protect delocalized spin-wave excitation, enabling long-lived quantum storage at the ‘magic’ magnetic field. At a storage time of 5.6 s, we achieve a time-bin qubit storage fidelity of $88.0 \pm 2.1\%$, surpassing the maximum fidelity attainable via classical strategies. Our device reaches a $1/e$ storage lifetime of 27.6 ± 0.5 s, enabling single-photon-level storage for 42 s with a signal-to-noise ratio greater than unity. This work establishes photonic quantum memory in the minute-scale regime, laying a solid foundation for global-scale quantum network and deep-space quantum experiments.

Quantum entanglement distribution is currently limited to 404 km in optical fibers [1] and 1200 km via a single low-Earth-orbit satellite [2]. Quantum repeaters [3, 4] provide a scalable path beyond these ranges by dividing the total communication distance into shorter elementary links, synchronized via long-lived quantum memories. Realizing a global-scale quantum network will require quantum storage times on the order of seconds to minutes [4–7]. Transportable quantum memories further broaden this vision by enabling worldwide quantum communication via the physical transport of stored quantum states, with target storage times approaching one hour [8, 9]. Similarly, foundational experiments with deep-space quantum links—such as Bell tests over astronomical baselines and studies of entanglement dynamics in gravitational fields—also require photonic storage times lasting seconds to minutes [10–12].

However, existing photonic quantum memories remain limited to subsecond storage times [13–16]. The current state of the art reaches a $1/e$ lifetime of approximately 0.1 s for absorptive-type quantum memories [13, 14] and 0.46 s for emissive-type systems [16], falling substantially short of the demands for global-scale quantum networks or advanced memory-assisted applications discussed above.

$\text{Eu}^{3+}:\text{Y}_2\text{SiO}_5$ crystals are a leading candidate for long-lived photonic quantum memory [14, 17–19], having demonstrated 1-hour storage of classical light at a ‘magic’ magnetic field featuring zero first-order Zeeman (ZEFOZ) effects [20]. Yet, the single-photon storage time

remains confined to 0.1 s, achieved at near-zero field to maintain adequate optical absorption [14]. This limitation arises because operation at the ZEFOZ magnetic field, while advantageous for spin coherence, markedly diminishes optical absorption owing to the full removal of level degeneracy. Exacerbating this challenge is the difficulty of implementing long-duration dynamical decoupling (DD) for a single delocalized spin-wave excitation. Consequently, the feasibility of long-lived quantum storage at the ZEFOZ magnetic field remains an open question [21].

In this work, we demonstrate a minute-scale photonic quantum memory by implementing the noiseless photon echo (NLPE) protocol [22] combined with a universally robust (UR) DD sequence [23] in $^{151}\text{Eu}^{3+}:\text{Y}_2\text{SiO}_5$ crystals under a ZEFOZ magnetic field [17]. The memory achieves a $1/e$ storage lifetime of 27.6 s—more than two orders of magnitude beyond previous records for absorptive photonic quantum memories [13, 14]. At a storage time of 5.6 s, it maintains an efficiency of 8.2% and delivers a qubit storage fidelity of $88.0 \pm 2.1\%$, unambiguously surpassing the classical bound.

Fig. 1 illustrates the experimental layout. The 580-nm laser is a frequency-doubled semiconductor laser (Top-Optica, TA-SHG) with a stabilized linewidth of approximately 1 kHz. Both the signal beam and the control beam are generated with double-passed acousto-optic modulators (AOMs). The control beam intersects the signal beam on the crystal at an angle of 1.5° , with full width at half maximum (FWHM) of 250 μm and

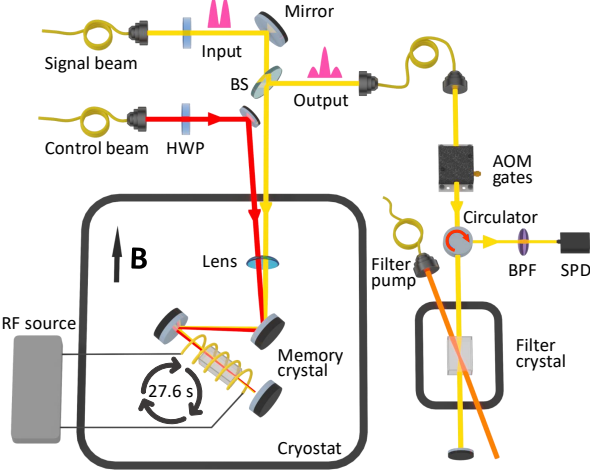


FIG. 1. Schematic of the experimental setup. The polarization of signal and control beams are controlled with half-wave plates (HWPs), to be polarized parallel to the D_1 axis of the memory crystal (MC) to maximize interaction strength. Both beams overlap inside the MC an angle of 1.5° . The signal beam propagates along the MC's b-axis, guided by three steering mirrors, and is retro-reflected along the same path. A 95(R):5(T) beam splitter (BS) separates the output signal, which is then coupled into a single-mode fiber. The MC is precisely aligned inside the magnet using two goniometer stages. Dynamical decoupling on the spin transitions is implemented by applying amplified RF pulses via solenoid coils surrounding the MC. Photonic time-bin encoded qubits are stored inside the MC with a $1/e$ lifetime of 27.6 s. The readout signal subsequently passes through a temporal gate based acousto-optic modulator (AOM), followed by spectral filtering with a double-passed filter crystal (FC) and a 0.5-nm band-pass filter (BPF). The FC is prepared by a pump beam to create a 0.8-MHz transparent spectral window centered at the signal frequency. The filtered signal is finally detected with a fiber-coupled single-photon detector (SPD).

100 μm for the control and signal beams, respectively. Both beams travel along the b-axis of the memory crystal (MC) with the polarization aligned to the D_1 -axis. The MC is a 0.01% $^{151}\text{Eu}^{3+}:\text{Y}_2\text{SiO}_5$ crystal with a size of $5 \times 4 \times 10 \text{ mm}^3$ along the $D_1 \times D_2 \times b$. A solenoid coil with a diameter of 10 mm and a length of 18 mm surrounding the MC supplies the RF field for spin manipulation. The MC is cooled to 1.65 K using a low-vibration close-cycle cryostat (Attodry 2100). After the double-passed MC, the read-out pulse is temporally gated by AOMs and spectrally filtered by a double-passed filter crystal (FC) housed in a separate homemade cryostat. The FC is a 15-mm-long $^{151}\text{Eu}^{3+}:\text{Y}_2\text{SiO}_5$ crystal with a dopant concentration of 0.1%. It is prepared with a 0.8-MHz-wide transparency window at the signal frequency, outside of which the absorption depth reaches 13.2.

In order to extend the spin coherence lifetime, the memory was operated at a ZEFOZ magnetic field of

$1.2968 \pm 0.0002 \text{ T}$, applied along the direction $[-0.544, -0.601, 0.586]$ in the crystal's $D_1 \times D_2 \times b$ coordinate frame [17, 20]. We note that the reported field strength has now been calibrated with an NMR teslameter (Metrolab, PT2026), thus representing an accurate value. The orientation of the MC is finely adjusted using two goniometer stages [20] to maximize the measured two-pulse spin coherence lifetime. After systematic optimization of the field magnitude and orientation, a two-pulse spin-echo coherence lifetime of $T_2 = 18.7 \pm 0.7 \text{ s}$ (Fig. 2c) was achieved for the ZEFOZ transition between states $|3\rangle_g$ and $|4\rangle_g$. The two-pulse spin echo T_2 reported here is shorter than those achieved with shorter crystals [17, 20], owing to the compromise in magnetic field homogeneity imposed by the 10-mm interaction length—necessary for efficient single-photon absorption—which in turn decreases the effective T_2 [24]. Employing a magnet with improved homogeneity would permit longer quantum storage times, as the two-pulse spin echo T_2 can be extended to approximately 50 s.

The application of a ZEFOZ magnetic field to $^{151}\text{Eu}^{3+}:\text{Y}_2\text{SiO}_5$ lifts all level degeneracies—including hyperfine doublets and magnetically inequivalent subsites—and consequently leads to a sharp reduction in optical absorption, measured here at approximately 0.5 cm^{-1} for the double-passed MC. In this regime, standard quantum memory protocols that depend on spectral tailoring [26, 27] to achieve atomic rephasing in an inhomogeneously broadened ensemble would suffer severe efficiency losses. We therefore adopt the NLPE protocol, which performs direct optical rephasing to make full use of the natural sample absorption for efficient quantum storage [22, 28–30].

	$ 1\rangle_e$	$ 2\rangle_e$	$ 3\rangle_e$	$ 4\rangle_e$	$ 5\rangle_e$	$ 6\rangle_e$
$ 1\rangle_g$	0.57	0.18	0.12	0.10	0.01	0.02
$ 2\rangle_g$	0.32	0.54	0.01	0.06	0.00	0.07
$ 3\rangle_g$	0.06	0.18	0.44	0.10	0.01	0.21
$ 4\rangle_g$	0.00	0.10	0.14	0.42	0.04	0.30
$ 5\rangle_g$	0.04	0.00	0.23	0.27	0.08	0.38
$ 6\rangle_g$	0.01	0.00	0.06	0.05	0.86	0.02

TABLE I. Branching ratio of optical transitions. Matrix representation of transition branching ratios between ground (columns) and excited (rows) states. Energy levels involved in the NLPE memory are highlighted in red.

We first calculate the energy level structure of $^{151}\text{Eu}^{3+}$ in Y_2SiO_5 crystal under the ZEFOZ magnetic field, as illustrated in Fig. 2a. The optical transition probabilities are listed in Tab. I which are calculated according to the hyperfine Hamiltonian of the ground and excited states provided in our previous work [31]. Implementation of NLPE protocol requires a four-level system whose two ground states are fixed to the ZEFOZ hyperfine transition $|3\rangle_g \leftrightarrow |4\rangle_g$. Among the optical transitions satisfying

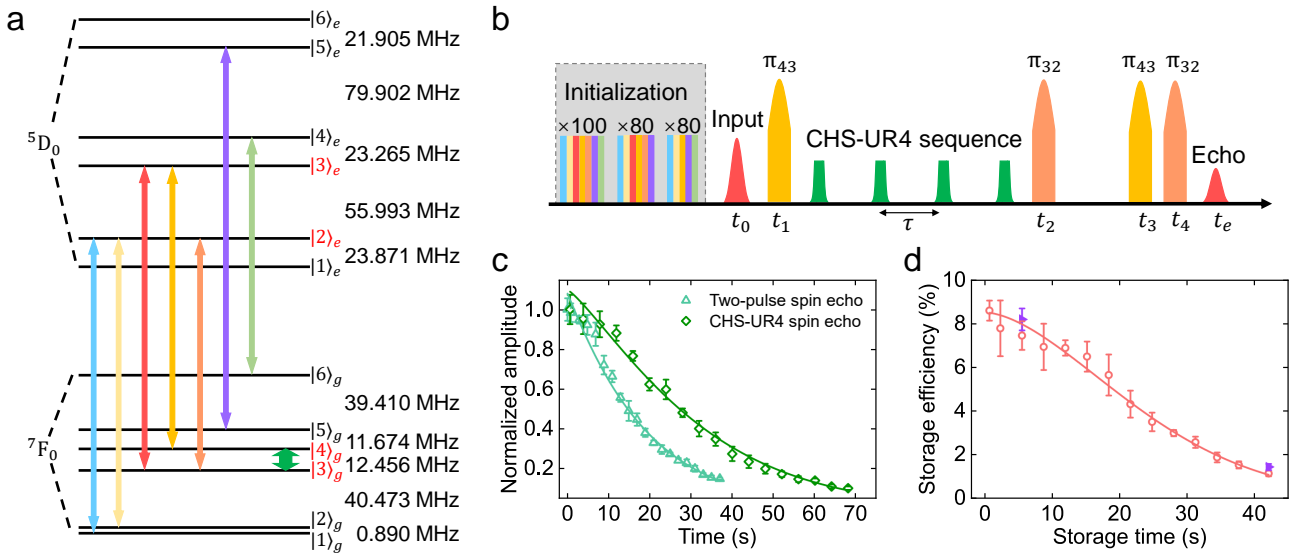


FIG. 2. Characterization of the long-lived quantum memory. **a.** Energy level structure of $^{151}\text{Eu}^{3+}$ in Y_2SiO_5 crystal under the ZEFOZ magnetic field of 1.2968 ± 0.0002 T. Colored lines represent optical and spin transitions: red for the signal beam, orange and coral for control beams; the green marker indicates the ZEFOZ spin transition at 12.456 MHz. **b.** Experimental sequence of the long-lived quantum memory. The gray region indicates initialization. This is followed by the NLPE-DD storage sequence, which employs a DD process based on the CHS-UR4 sequence. The final photonic echo is emitted at $t_e = t_4 + t_3 - t_2 - t_1 + t_0$. **c.** Decay of spin echo amplitude with total evolution time for two-pulse spin echo (triangle) and the CHS-UR4 sequences (diamond). Spin echoes are detected via pulsed Raman heterodyne detection [20]. The data are fitted to Mims' equation $e^{-(t/T_2)^m}$ [25], yielding $T_2 = 18.7$ s, $m = 1.05$ for the two-pulse spin echo, and $T_2 = 33.1$ s, $m = 1.25$ for the CHS-UR4 sequence. **d.** Photonic storage efficiency of the NLPE-DD memory as a function of storage time. The data are fitted to $e^{-(t/T_M)^m}$ with $T_M = 27.6 \pm 0.5$ s and $m = 1.70$. Red circles denote measurements using classical light; purple triangles represent single-photon-level inputs. The slightly higher efficiency in single-photon measurements results from the uncorrected contribution from noise counts, which are negligible under classical inputs. All error bars indicate ± 1 standard deviation throughout.

this constraint, the $|3\rangle_g \leftrightarrow |3\rangle_e$ line, which provides the highest transition strength, is selected as the signal transition. For the auxiliary excited state, we choose $|2\rangle_e$ because its transition to $|3\rangle_g$ is strong, while the $|4\rangle_g \leftrightarrow |2\rangle_e$ transition is weak; this asymmetry helps to suppress spontaneous-emission noise from the fully populated $|2\rangle_e$ level during the NLPE sequence [22].

Fig. 2b sketches the time sequence of our long-lived photonic quantum memory. Initialization proceeds in three steps. First, a class-cleaning sequence [22, 32] selects a class of ions within a 3 MHz bandwidth. Second, spin polarization [22, 32] transfers all these ions to $|6\rangle_g$. Finally, five chirped pulses (0.8 MHz bandwidth) centered at f_{12} , f_{22} , f_{43} , f_{55} , and f_{64} back-pump the ions into the target $|3\rangle_g$, where f_{ij} represents the transition frequency for $|i\rangle_g \leftrightarrow |j\rangle_e$. Following the initialization sequence, we obtain an absorption feature centered on the $|3\rangle_g \leftrightarrow |3\rangle_e$ transition, with a width of 0.8 MHz, a depth of 1.0, and located within a 3 MHz transparency window.

The input signal, centered at frequency f_{33} and injected at time t_0 , is a truncated Gaussian pulse with a total duration of 3 μs and a FWHM of 1.5 μs . The NLPE protocol requires four optical π pulses to perform direct optical rephasing in the inhomogeneously broad-

ened ensemble. To this end, we implement four adiabatic complex-hyperbolic-secant (CHS) pulses [22, 33], which enable efficient and uniform π rotations across the entire ensemble. The first π_{43} pulse maps the optical signal onto the spin-wave excitation between states $|3\rangle_g \leftrightarrow |4\rangle_g$. A subsequent π_{32} pulse converts this spin coherence into an optical coherence between $|2\rangle_e \leftrightarrow |4\rangle_g$. A second pair of π_{43} and π_{32} pulses then retrieves the optical echo signal at frequency f_{33} [29]. Since all population is eventually returned to the ground states and fluorescence from $|2\rangle_e$ is spectrally distinct from the signal, the final echo is emitted free from noise in principle. Here, π_{mn} denotes a π pulse driving the transition $|m\rangle_g \leftrightarrow |n\rangle_e$.

Extending the spin-wave storage lifetime for arbitrary photonic states requires a robust DD sequence that is insensitive to the initial state and immune to pulse errors. To this end, we implement a UR4 DD sequence [23] and replace all rectangular π -pulses with adiabatic CHS RF pulses [33, 34], achieving optimized protection of the spin-wave quantum excitation. Furthermore, since the precise spacing between CHS pulses directly dictates the effective phase relationship—and thus the performance—of the UR4 sequence (see Supplementary Information for detailed analysis), we employ a rubidium fre-

quency standard as the master time reference for pulse generation to ensure timing accuracy. This CHS-UR4 hybrid achieves optimal transfer efficiency while minimizing pulse-error-induced noise, obtaining a UR4 spin T_2 of 33.1 ± 1.6 s (Fig. 2c). Then we combine the NLPE memory with DD by applying the CHS-UR4 sequence after the first optical π_{43} pulse (Fig. 2b), achieving a $1/e$ quantum storage lifetime of $T_M = 27.6 \pm 0.5$ s for the NLPE-DD memory (Fig. 2d). To reduce integration time, most of the data are collected with classical light which agrees well with the single-photon data shown with purple triangles. We have observed that shorter DD pulse intervals caused notable RF-induced heating, degrading optical coherence and storage efficiency at short storage times. Consequently, the measured T_M and the Mims factor m [25] differ from the values extracted from the CHS-UR4 spin echo fitting, with further discussion provided in the Supplementary Information.

Fig. 3a displays the photon counting histogram for the NLPE memory using weak coherent input pulses carrying a mean photon number of $\mu = 1.18$ per pulse. Within a 2.1 μ s detection window, the measured storage efficiency is $9.65 \pm 0.5\%$ and a noise level of $0.17 \pm 0.07\%$, yielding a signal-to-noise ratio (SNR) of 65.2 ± 27.2 at a storage time of 28.1 μ s. Throughout this paper, the SNR are calculated using the noise-subtracted signal counts measured inside the detection window. Fig. 3b shows the corresponding histogram for the NLPE-DD memory under the same input conditions, using a DD pulse interval of $\tau = 1.4$ s. At a readout time of 5.600032 s, the storage efficiency is $8.2 \pm 0.5\%$, with a SNR of 11.3 ± 2.5 . Although the NLPE-DD memory maintains an efficiency comparable to that of the NLPE memory—reflecting the high rephasing efficiency of the CHS-UR4 sequence—the observed reduction in SNR stems from an increase in noise. This increased noise originates from imperfections in the CHS-UR4 sequence across the large ensemble, which leave residual population in the $|4\rangle_g$ after DD. This residual population is subsequently excited to $|3\rangle_e$ by the second π_{43} pulse, leading to spontaneous emission noise. Despite this, the SNR achieved here is comparable to those of quantum memories incorporating DD at zero or low magnetic fields [14, 30], while extending the storage time by more than two orders of magnitude.

To demonstrate that our device indeed works in the quantum regime, we encode the inputs with time-bin qubits [22, 35]. The four input qubit states are $|e\rangle$, $|l\rangle$, $|e\rangle + |l\rangle$ and $|e\rangle + i|l\rangle$, where $|e\rangle$ and $|l\rangle$ correspond to the early and late time bins, respectively. Each pulse retains identical parameters to those used in earlier tests, with a fixed separation of 3 μ s between $|e\rangle$ and $|l\rangle$. The eigen states $|e\rangle$ and $|l\rangle$ can be directly analyzed with standard NLPE-DD sequence. To analyze the superposition states, we split the second optical π_{32} pulse into two $\pi/2$ pulses separated by 3 μ s, to read out the signal twice

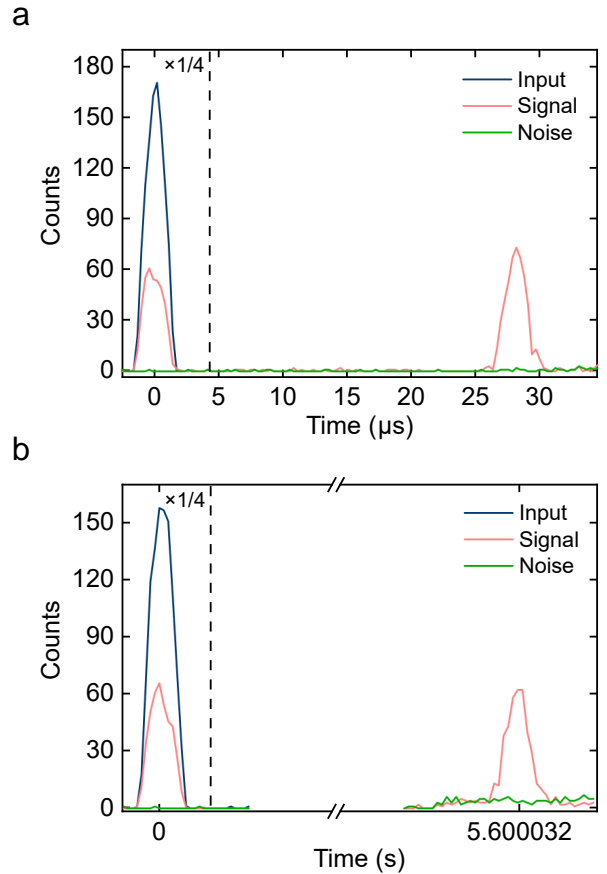


FIG. 3. **Storage of single-photon level inputs.** a and b. Photon counting histogram of NLPE memory (a) and NLPE-DD memory (b), measured using weak coherent input pulses with a mean photon number $\mu = 1.18$ and integrated over 35,000 experimental trials. The blue, red, and green curves denote the input photon counts, output signal, and noise level (measured without input), respectively. For clarity, data to the left of the dashed line are scaled down by a factor of 4. The shaded region indicates the 2.1 μ s detection window, yields SNRs of 65.2 ± 27.2 and 11.3 ± 2.5 at readout times of 28.1 μ s and 5.600032 s, respectively.

to effectively mimic the function of unbalanced Mach-Zehnder interferometer [22]. By tuning the phase between the two $\pi/2$ pulses, we modulate the interference of outputs to accomplish the analysis of the superposition states. The average photon number per qubit (μ_q) is 1.16. Photon counting histograms for the four input qubits are presented in Fig. 4 with a storage time of 5.600032 s.

We denote the fidelity of input qubit $|i\rangle$ as $F_{|i\rangle}$. The total fidelity is computed as $F_t = \frac{1}{3} \frac{F_{|e\rangle} + F_{|l\rangle}}{2} + \frac{2 F_{|e\rangle + |l\rangle} + F_{|e\rangle + i|l\rangle}}{3} \frac{2}{2}$. Here, the basis-state fidelities $F_{|e\rangle}$ and $F_{|l\rangle}$ are calculated as $\frac{S+N}{S+2N}$, where S denotes the signal counts (noise excluded) and N denotes the noise counts. Specifically for $F_{|e\rangle}$, $S+N$ and N correspond, respectively, to the measured counts in the target time bin $|e\rangle$ and the counts in the orthogonal time bin $|l\rangle$.

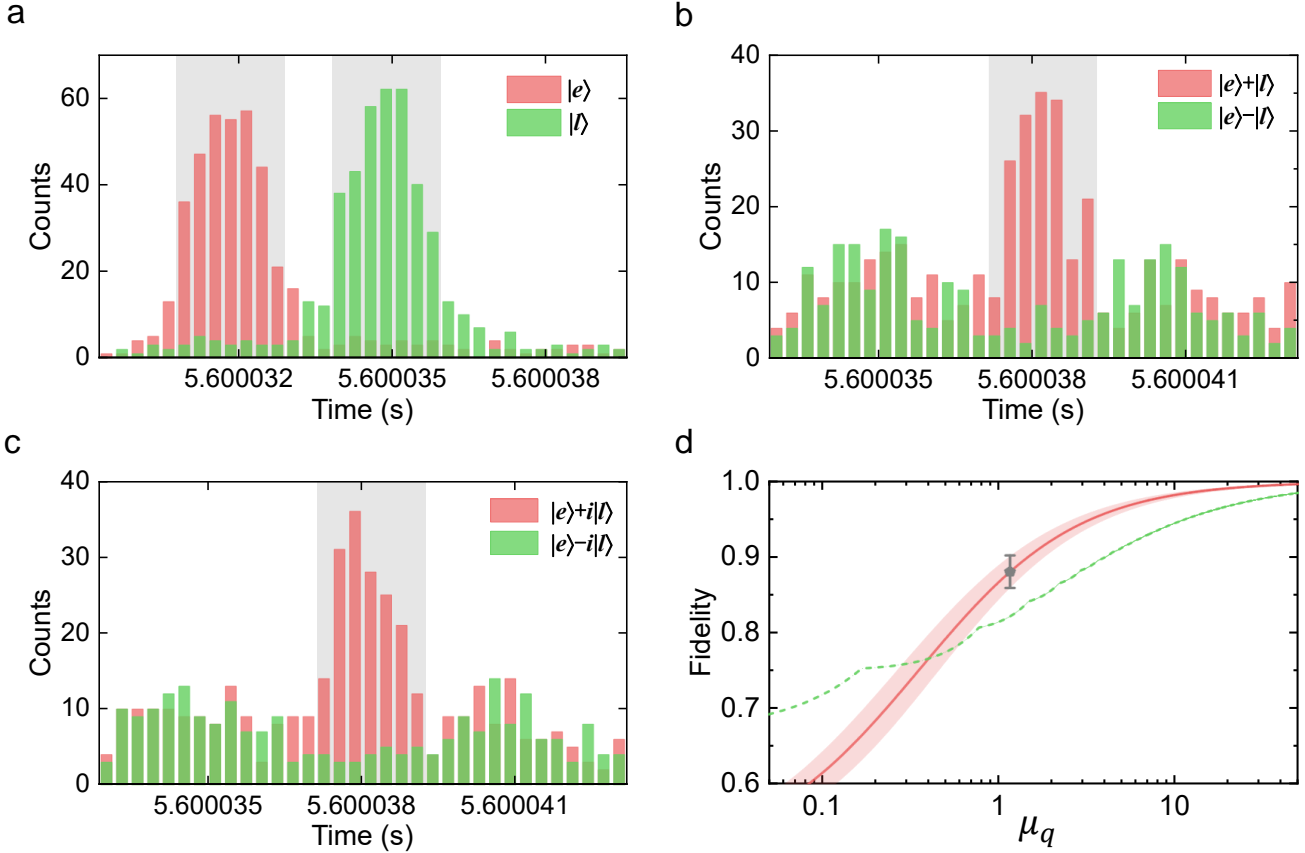


FIG. 4. **Storage of time-bin qubits for 5.600032 s.** **a.** Photon counting histogram for the input qubits $|e\rangle$ and $|l\rangle$. Output counts for $|e\rangle$ and $|l\rangle$ are shown as red and green bars, respectively. The gray-shaded region marks the 2.1 μ s detection window. The mean input photon number per qubit is $\mu_q = 1.16$, integrated over 35,000 experimental trials. The measured fidelities are $F_{|e\rangle} = 92.7 \pm 1.4\%$ and $F_{|l\rangle} = 92.7 \pm 1.4\%$. **b,c.** Photon counting histogram for the input qubit $|e\rangle + |l\rangle$ and $|e\rangle + i|l\rangle$, red and green bars correspond to constructive and destructive interference measurements for each qubit. All other experimental settings match those in **a**. The measured fidelities are $F_{|e\rangle+|l\rangle} = 85.8 \pm 2.5\%$ and $F_{|e\rangle+i|l\rangle} = 85.6 \pm 2.5\%$. **d.** Classical fidelity limit for memory as a function of μ_q . The green dashed line indicates the classical bound for a measure-and-prepare strategy under 8.2% storage efficiency. The gray dot marks the measured memory fidelity of $88.0 \pm 2.1\%$ at $\mu_q = 1.16$. The solid red line represents the expected fidelity calculated from the experimentally determined efficiency and noise.

The superposition-state fidelities $F_{|e\rangle+|l\rangle}$ and $F_{|e\rangle+i|l\rangle}$ are evaluated as $\frac{V+1}{2}$, where $V = \frac{c_{max}-c_{min}}{c_{max}+c_{min}}$ is the interference visibility, with c_{max} and c_{min} representing the photon counts in the central time bin under constructive and destructive interference conditions, respectively. The measured storage fidelities are provided in Fig. 4, which give a F_t of $88.0 \pm 2.1\%$. We calculate the maximal storage fidelity that can be achieved using classical prepare-and-measure strategy which takes into account the finite storage efficiency and the Poisson statistics of input coherent states [35, 36]. The green dashed line in Fig. 4d represents this classical fidelity bound while the red solid line represents the expected storage fidelity of our device calculated according to the storage efficiency and measured noise. The measured fidelity F_t at 5.600032 s violates the classical bound (82.1%) by 2.8 standard deviations, unambiguously demonstrating this

device operating in the true quantum regime. The cross over between these two lines indicates that our device operating beyond the classical limit with a minimal μ_q of 0.41.

The fundamental fidelity limit for a quantum memory using true single-photon (Fock-state) inputs is $2/3$ [37], equivalently requiring an SNR of 1:1. To probe the fundamental performance limits of our device, we extended the storage time to 42.000032 s by adjusting the CHS-UR4 pulse spacing to $\tau = 10.5$ s (Fig. 5). To reduce integration time, measurements were conducted using an input qubit $|l\rangle$ with $\mu_q = 4.14$. The measured SNR of 5.54 ± 1.38 corresponds to a single-photon-equivalent SNR of 1.34 ± 0.33 , which remains above the operational threshold for a quantum memory operating with ideal single-photon inputs. The reduction in SNR at longer storage times primarily results from the decay of storage efficiency—

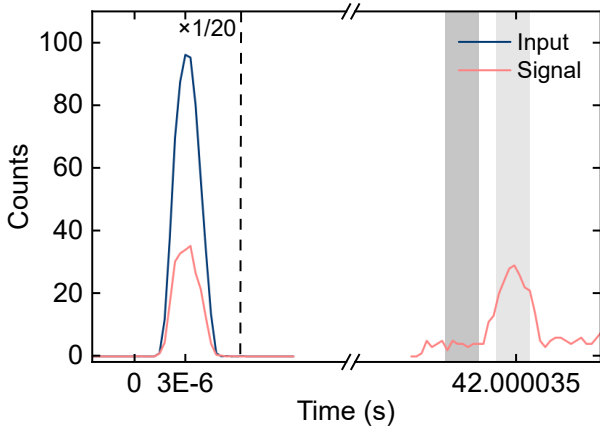


FIG. 5. **Storage of qubit $|l\rangle$ for 42.000032 s.** Photon counting histogram of the input qubit $|l\rangle$ encoded with weak coherent pulses with $\mu_q = 4.14$, accumulated over 28,000 experimental trials. The blue curve indicates the input photon counts, and the red curve shows the storage process. For visual clarity, photon counts to the left of the vertical dashed line are scaled down by a factor of 20. The dark and light shaded regions mark the detection windows for the orthogonal time bin $|e\rangle$ and target time bin $|l\rangle$, respectively.

which drops to 1.47% at 42.000032 s (Fig. 2d)—while the noise floor remains nearly unchanged. This noise stability is achieved because the dominant noise source—residual population induced by the DD sequence—depends solely on the number of RF pulses applied, regardless of the interval between them. This behavior further confirms the successful minute-scale implementation of the UR4 DD sequence. Addressing the efficiency-noise trade-off in longer DD sequences will be pivotal to unlocking further gains in performance.

By implementing an NLPE-DD protocol in a $^{151}\text{Eu}^{3+}:\text{Y}_2\text{SiO}_5$ crystal at a ZEFOZ magnetic field, we have realized a photonic quantum memory with a $1/e$ lifetime of $T_M = 27.6 \pm 0.5$ s. The memory preserves photonic time-bin qubits beyond the classical fidelity limit after 5.6 s of storage—marking a 280-fold improvement over prior long-lived absorptive quantum memories [14] and fulfilling a key requirement for global-scale quantum repeater networks [5–7] and fundamental physical tests with deep-space quantum links [10, 11].

Further extending the storage lifetime is essential for applications such as transportable quantum memories [8, 9] and quantum communication across interplanetary or inter-spacecraft links [12]. A storage time of several minutes can be straightforwardly achieved using a magnet with improved field homogeneity [24]. Substantially longer coherence can be attained by using $^{153}\text{Eu}^{3+}$ ions, which are expected to exhibit extended two-pulse spin echo T_2 due to their smaller magnetic g -tensor and reduced sensitivity to magnetic noise. Additional gains are feasible through the optimization of DD sequences with more pulses and the growth of higher-quality crystals

[24]. Furthermore, near-unity storage efficiency could be reached by coupling the memory to an impedance-matched optical cavity [18], fully overcoming the weak-absorption constraint.

These advances position $\text{Eu}^{3+}:\text{Y}_2\text{SiO}_5$ crystals operating at ZEFOZ magnetic fields as the foundational hardware for large-scale quantum repeater networks whose transportable memories serve as mobile nodes, ushering in a flexible quantum architecture that mirrors today’s classical telecom infrastructure.

* zq_zhou@ustc.edu.cn

- [1] Zhuang, S.-C. *et al.* Ultrabright entanglement based quantum key distribution over a 404 km optical fiber. *Phys. Rev. Lett.* **134**, 230801 (2025).
- [2] Yin, J. *et al.* Satellite-based entanglement distribution over 1200 kilometers. *Science* **356**, 1140–1144 (2017).
- [3] Briegel, H.-J., Dür, W., Cirac, J. I. & Zoller, P. Quantum repeaters: The role of imperfect local operations in quantum communication. *Phys. Rev. Lett.* **81**, 5932–5935 (1998).
- [4] Sangouard, N., Simon, C., de Riedmatten, H. & Gisin, N. Quantum repeaters based on atomic ensembles and linear optics. *Rev. Mod. Phys.* **83**, 33–80 (2011).
- [5] Gündoğan, M. *et al.* Proposal for space-borne quantum memories for global quantum networking. *npj Quantum Information* **7**, 128 (2021).
- [6] Liu, P.-X., Lin, Y.-P., Zhou, Z.-Q., Li, C.-F. & Guo, G.-C. Global-scale quantum networking using hybrid-channel quantum repeaters with relays based on a chain of balloons. *arXiv:2507.15178 [quant-ph]* (2025).
- [7] Tubio, V. D., Aldecocea, M., van Dam, J., Sørensen, A. & Borregaard, J. Satellite-assisted quantum communication with single photon sources and atomic memories. *arXiv:2411.09533 [quant-ph]* (2024).
- [8] Gündoğan, M., Sidhu, J. S., Krutzik, M. & Oi, D. K. L. Time-delayed single satellite quantum repeater node for global quantum communications. *Optica Quantum* **2**, 140–147 (2024).
- [9] Bland-Hawthorn, J., Sellars, M. J. & Bartholomew, J. G. Quantum memories and the double-slit experiment: implications for astronomical interferometry. *J. Opt. Soc. Am. B* **38**, A86–A98 (2021).
- [10] Mol, J.-M. *et al.* Quantum memories for fundamental science in space. *Quantum Science and Technology* **8**, 024006 (2023).
- [11] Barzel, R., Gündoğan, M., Krutzik, M., Rätzel, D. & Lämmerzahl, C. Entanglement dynamics of photon pairs and quantum memories in the gravitational field of the earth. *Quantum* **8**, 1273 (2024).
- [12] Mohageg, M. *et al.* The deep space quantum link: prospective fundamental physics experiments using long-baseline quantum optics. *EPJ Quantum Technology* **9**, 25 (2022).
- [13] Körber, M. *et al.* Decoherence-protected memory for a single-photon qubit. *Nat. Photon.* **12**, 18–21 (2018).
- [14] Ortú, A., Holzapfel, A., Etesse, J. & Afzelius, M. Storage of photonic time-bin qubits for up to 20 ms in a rare-earth doped crystal. *npj Quantum Information* **8**, 29 (2022).

[15] Yang, S.-J., Wang, X.-J., Bao, X.-H. & Pan, J.-W. An efficient quantum light-matter interface with sub-second lifetime. *Nat. Photon.* **10**, 381–384 (2016).

[16] Wang, X.-J. *et al.* Cavity-enhanced atom-photon entanglement with subsecond lifetime. *Phys. Rev. Lett.* **126**, 090501 (2021).

[17] Zhong, M. *et al.* Optically addressable nuclear spins in a solid with a six-hour coherence time. *Nature* **517**, 177–180 (2015).

[18] Meng, R.-R. *et al.* Efficient integrated quantum memory for light. *arXiv:2511.05928 [quant-ph]* (2025).

[19] Zhu, T.-X. *et al.* A metropolitan-scale multiplexed quantum repeater with bell nonlocality. *arXiv:2508.17940 [quant-ph]* (2025).

[20] Ma, Y., Ma, Y.-Z., Zhou, Z.-Q., Li, C.-F. & Guo, G.-C. One-hour coherent optical storage in an atomic frequency comb memory. *Nat. Commun.* **12**, 2381 (2021).

[21] Afzelius, M., Gisin, N. & de Riedmatten, H. Quantum memory for photons. *Physics Today* **68**, 42 (2015).

[22] Ma, Y.-Z. *et al.* Elimination of noise in optically rephased photon echoes. *Nat. Commun.* **12**, 4378 (2021).

[23] Genov, G. T., Schraft, D., Vitanov, N. V. & Halfmann, T. Arbitrarily accurate pulse sequences for robust dynamical decoupling. *Phys. Rev. Lett.* **118**, 133202 (2017).

[24] Ma, Y.-Z. *et al.* Monte Carlo simulation of the nuclear spin decoherence process in $\text{Eu}^{3+}:\text{Y}_2\text{SiO}_5$ crystals. *Phys. Rev. B* **107**, 014310 (2023).

[25] Mims, W. B. Phase Memory in Electron Spin Echoes, Lattice Relaxation Effects in CaWO_4 : Er, Ce, Mn. *Phys. Rev.* **168**, 370–389 (1968).

[26] de Riedmatten, H., Afzelius, M., Staudt, M. U., Simon, C. & Gisin, N. A solid-state light-matter interface at the single-photon level. *Nature* **456**, 773–777 (2008).

[27] Hedges, M. P., Longdell, J. J., Li, Y. & Sellars, M. J. Efficient quantum memory for light. *Nature* **465**, 1052–1056 (2010).

[28] Jin, M., Ma, Y.-Z., Zhou, Z.-Q., Li, C.-F. & Guo, G.-C. A faithful solid-state spin-wave quantum memory for polarization qubits. *Science Bulletin* **67**, 676–678 (2022).

[29] Zhu, T.-X. *et al.* Integrated spin-wave quantum memory. *Nat. Sci. Rev.* **11**, nwae161 (2024).

[30] Liu, Y.-P. *et al.* A millisecond integrated quantum memory for photonic qubits. *Sci. Adv.* **11**, eadu5264 (2025).

[31] Ma, Y. *et al.* A Raman heterodyne study of the hyperfine interaction of the optically-excited state ${}^5\text{D}_0$ of $\text{Eu}^{3+}:\text{Y}_2\text{SiO}_5$. *Journal of Luminescence* **202**, 32–37 (2018).

[32] Lauritzen, B. *et al.* Spectroscopic investigations of $\text{Eu}^{3+}:\text{Y}_2\text{SiO}_5$ for quantum memory applications. *Phys. Rev. B* **85**, 115111 (2012).

[33] Roos, I. & Mølmer, K. Quantum computing with an inhomogeneously broadened ensemble of ions: Suppression of errors from detuning variations by specially adapted pulses and coherent population trapping. *Phys. Rev. A* **69**, 022321 (2004).

[34] Pascual-Winter, M. F., Tongning, R.-C., Chanelière, T. & Gouët, J.-L. L. Securing coherence rephasing with a pair of adiabatic rapid passages. *New J. Phys.* **15**, 055024 (2013).

[35] Gündoğan, M., Ledingham, P. M., Kutluer, K., Mazzera, M. & de Riedmatten, H. Solid state spin-wave quantum memory for time-bin qubits. *Phys. Rev. Lett.* **114**, 230501 (2015).

[36] Specht, H. P. *et al.* A single-atom quantum memory. *Nature* **473**, 190–193 (2011).

[37] Massar, S. & Popescu, S. Optimal extraction of information from finite quantum ensembles. *Phys. Rev. Lett.* **74**, 1259–1263 (1995).

[38] Souza, A. M., Álvarez, G. A. & Suter, D. Robust dynamical decoupling. *Phil. Trans. R. Soc. A* **370**, 4748–4769 (2012).

[39] Gullion, T., Baker, D. B. & Conradi, M. S. New, compensated Carr-Purcell sequences. *Journal of Magnetic Resonance* (1969) **89**, 479–484 (1990).

Acknowledgments: This work is supported by the National Natural Science Foundation of China (Nos. 12222411 and 11821404) and the Quantum Science and Technology-National Science and Technology Major Project (No. 2021ZD0301200). Z.-Q.Z acknowledges the support from the Youth Innovation Promotion Association CAS.

Author contributions: Z.-Q.Z. designed the experiment and supervised all aspects of this work; Y.-C.L. performed the experiment and analyzed the data with the help from Y.-J.Z.; Y.-C.L. and Z.-Q.Z. wrote the manuscript; Z.-Q.Z. and C.-F.L. supervised the project. All authors discussed the experimental procedures and results.

Competing interests: The authors declare that they have no competing interests.

Data and materials availability: All data needed to evaluate the conclusions in the article are present in the paper or the supplementary materials.

SUPPLEMENTARY TEXT

Experimental details

Fig. S1a shows the details about the sample space inside the memory-crystal (MC) cryostat. The MC is mounted in an acrylic sample holder mounted on two goniometers for magnetic-field alignment. The mirror placed in front of the MC with two-axis adjustment ensures the signal beam to propagate along the b-axis the MC. This optical configuration is crucial to ensure that the control light experience no birefringence, thereby enabling the application of ideal optical π pulses for the MC in principle. A final mirror reflects the signal back through the MC, doubling the effective absorption length in a double-pass configuration. The control beam has a peak power of 320 mW at the crystal, reduced to 100 μ W during initialization. The signal beam operates at a peak power of 600 μ W and can be attenuated to the single-photon level using removable neutral density filters. The diameters of the control and signal beams at the center of the MC are approximately 250 μ m and 100 μ m.

The incident signal power on the crystal is given by $\sqrt{W_1 * W_2} / 0.95$, where W_1 and W_2 denote the optical power measured before the cryostat and after the 95(R):5(T) beam splitter, respectively. This calibration procedure is consistently applied in both bright and single-photon-level measurements. A vibration sensor attached to the cryostat monitors the mechanical vibrations and generates a synchronization signal to initiate the experiment. This step ensures that the storage and readout process always occurs in a low-vibration window of the cryostat. Continuous operation of the storage and readout process can also be achieved by using dedicated vibration-isolation sample holders, as demonstrated in our previous work [19].

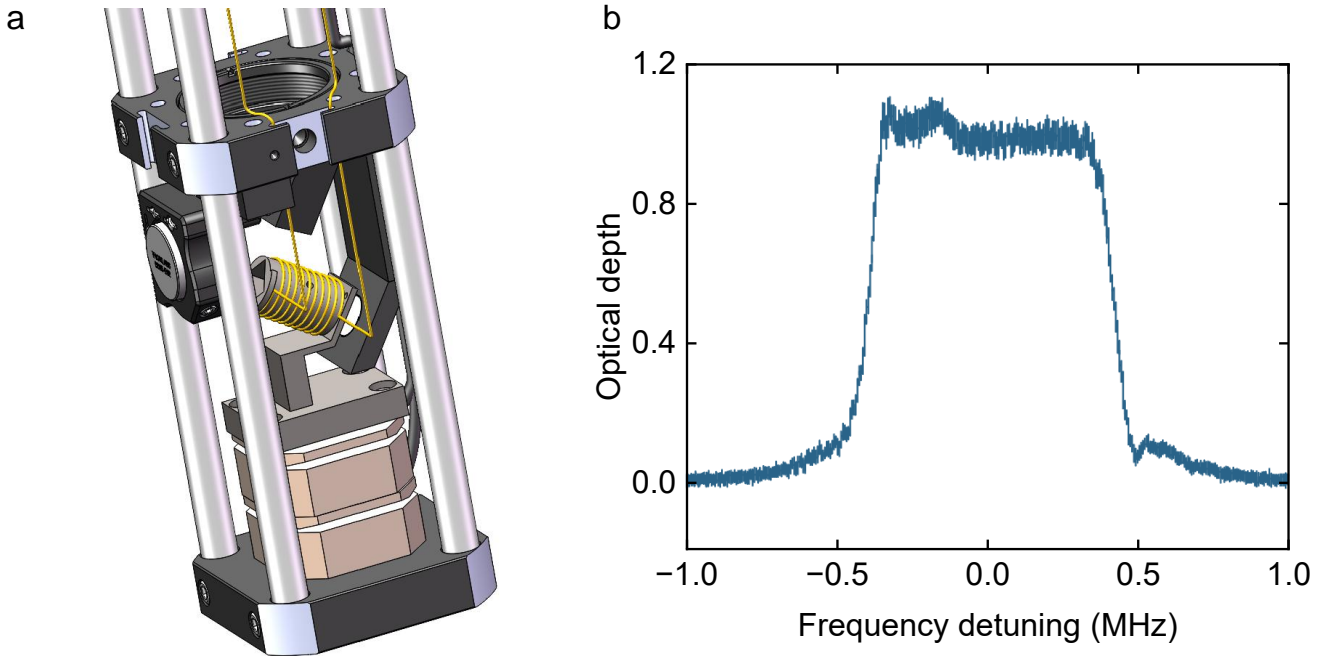


Fig. S1. **Details about the sample space and the absorption structure of MC.** **a.** Three-dimensional simulated schematic of the sample space inside the MC-cryostat. **b.** The absorption profile of the MC after initialization process with zero detuning corresponding to the center of the $|3\rangle_g \leftrightarrow |3\rangle_e$ transition.

Once the experiment begins, a chirped rectangular pulse centered at the signal frequency, with a bandwidth of 0.8 MHz, a duration of 1 ms, and a power of 60 μ W, is applied 200 times to the filtering crystal, generating a 0.8 MHz transparency window. The MC is then initialized through a sequence of class cleaning, spin polarization, and backburning steps [32]. First, six chirped pulses (each with 3 MHz bandwidth, 1 ms duration) centered at frequencies f_{12} , f_{22} , f_{33} , f_{43} , f_{55} , and f_{64} are applied to pump the six ground-state spin levels, where f_{ij} represents the transition frequency for $|i\rangle_g \leftrightarrow |j\rangle_e$. Meanwhile, a chirped pulse centered at f_{32} with the same parameters empties the frequency channel corresponding to the π_{32} pulse. This sequence is repeated 100 times to selectively prepare a spectrally defined ion class. Subsequently, the pulse at f_{64} is removed and the sequence is repeated 80 times to spin-polarize ions into state $|6\rangle_g$. Finally, inally, five chirped pulses (0.8 MHz bandwidth, 1 ms duration) at f_{12} , f_{22} , f_{43} , f_{55} , and f_{64} are

applied 80 times to back-pump the ions into the target state $|3\rangle_g$. In total, the initialization process for the MC takes a time of 1.580 s, which results in an isolated 0.8 MHz absorption feature on the $|3\rangle_g \leftrightarrow |3\rangle_e$ transition in the MC, as shown in Fig. S1b. The four optical π -pulses for the NLPE protocol are implemented using adiabatic CHS pulses [22, 33]. The π_{43} pulse has a duration of 4.1 μ s, a bandwidth of 0.8 MHz, and a peak power of 320 mW, while the π_{32} pulse has a duration of 3.9 μ s, a bandwidth of 0.8 MHz, and a peak power of 320 mW.

Characterization of NLPE protocol storage efficiency

The storage efficiency of the NLPE memory can be modeled as [29]:

$$\eta = d^2 e^{-d} (\eta_{\text{control}})^4 e^{-\frac{\Gamma_{34}^2 t_{31}^2}{2 \ln 2 / \pi^2}} e^{-\frac{\Gamma_{23}^2 t_{42}^2}{2 \ln 2 / \pi^2} - 2\gamma t_{42}}, \quad (\text{S1})$$

where d denotes the effective absorption depth after initialization, η_{control} represents the transfer efficiency of each optical π -pulses, t_{kl} represents the time interval between the k -th π -pulse and the l -th π -pulse., Γ_{34} is the inhomogeneous broadening of the $|3\rangle_g \leftrightarrow |4\rangle_g$ transition, Γ_{23} is the inhomogeneous broadening of the $|2\rangle_e \leftrightarrow |3\rangle_e$ transition, and γ is the effective optical decoherence rate. We measure the decay of the NLPE echo as a function of t_{31} and t_{42} (Fig. S2), and obtain the fitting results using Eq. S1: $\Gamma_{34} = 7.7 \pm 0.1$ kHz, $\Gamma_{23} = 8.4 \pm 0.5$ kHz, $\gamma = 5.9 \pm 1.8$ kHz. After substituting the measured η and d , we obtain $\eta_{\text{control}} = 82\%$ for the transfer efficiency of the optical π -pulses. The observed reduction in transfer efficiency, compared to the zero-field NLPE memory [22, 29], is due to the vertically reflected double-pass configuration used here, where the signal beam is focused onto the mirror rather than at the center of the MC. Consequently, the beam diameter increases within the crystal, degrading spatial overlap with the control beam. This can be mitigated in future designs by using a dual-window cryostat, or by adopting an integrated waveguide architecture [29].

In the NLPE-DD memory, when the DD pulse intervals are short, RF-induced heating becomes significant, leading to degradation of the optical storage efficiency at short storage times. As a result, only the $1/e$ storage lifetime can be extracted from the efficiency decay curve (as shown in Fig. 2d of the main text), and the spin-coherence time T_2^{spin} cannot be reliably determined through fitting of optical storage efficiency. To mitigate the influence of RF heating, we perform fitting only on data points with storage times longer than 15 s (Fig. S2c), where heating effects are no longer significant. The fit yields a spin-coherence time of $T_2^{\text{spin}} = 36.3 \pm 2.4$ s with a Mims factor of $m = 1.25$, which is consistent with the CHS-UR4 spin-echo T_2 reported in the main text.

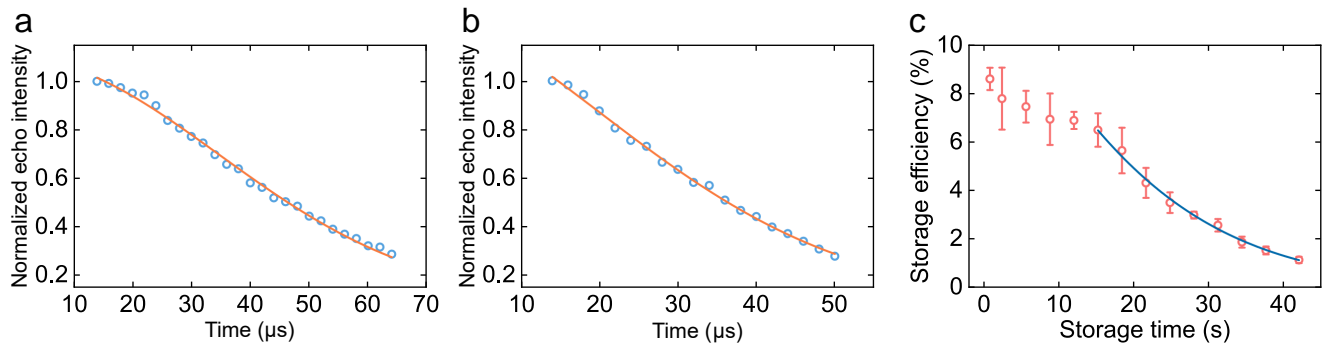


Fig. S2. Efficiency decay of the NLPE memory. **a, b.** NLPE echo intensity as a function of t_{31} (a) and t_{42} (b). The blue circles represent the measured values, and the orange curve represents the fit based on Eq. S1. **c.** The NLPE-DD memory efficiency versus storage times. Data after 15 s is fitted with Mims model $e^{-2(t/T_2^{\text{spin}})^m}$ [25], yielding $T_2^{\text{spin}} = 36.3 \pm 2.4$ s and $m = 1.25$.

The CHS-UR4 sequence

The performance of DD over an ensemble-based quantum memory is fundamentally determined by the quality of the individual pulses, the noise-suppression capability of the sequence, and its robustness to pulse errors. In practice, the dominant limitation of DD is pulse imperfections, often exceeding the impact of environmental noise [38]. This is especially true for our large, spectrally broadened atomic ensemble. The UR sequences achieve highly robust DD by engineering the pulse phases so that pulse-error contributions cancel at the sequence level, while offering arbitrary-order compensation against slowly changing environmental dephasing. In principle, they can compensate pulse errors originating from any experimental parameter and remain compatible with arbitrary pulse shapes [23]. To minimize noise associated with a large number of pulses, here we employ the simplest variant, the UR4 sequence. For rectangular π -pulses, the phases of the UR4 sequence are given by 0, ϕ_2 , $\pi + 2\phi_2$, and $3\pi + 3\phi_2$, where ϕ_2 is an arbitrary variable.

In practice, the performance of rectangular π -pulses is limited by their narrow bandwidth and sensitivity to pulse errors, particularly given the weak nuclear spin transition and limited RF power available. We therefore replace them with more robust adiabatic CHS pulses [33, 34]. However, because the phase of a CHS pulse is defined differently from that of a rectangular π -pulse, further clarification is necessary. The CHS pulse is described by:

$$\Omega_0 \operatorname{sech}(\beta t) \cos[\omega_c t - \mu \ln(\operatorname{sech}(\beta t)) + \phi_0], \quad (\text{S2})$$

where Ω_0 is the maximum Rabi frequency, β characterizes the FWHM of the pulse, μ is the chirp strength parameter, ϕ_0 denotes the constant phase, and t ranges from $-\frac{T}{2}$ to $\frac{T}{2}$, with T representing the pulse duration. From the Eq. S2, the CHS pulse has an amplitude envelope $\Omega(t) = \Omega_0 \operatorname{sech}(\beta t)$ and a dynamic phase $\phi(t) = -\mu \ln(\operatorname{sech}(\beta t)) + \phi_0$. Previous studies indicate that, under adiabatic conditions, an adiabatic rapid passage (ARP) produces the same effect as a π -rotation of the Bloch vector about an axis located in the xy-plane of the Bloch sphere [34]. The phase of the rotation axis can be written as:

$$\phi_0^{\text{ARP}} = \frac{\pi}{2} - \frac{1}{2} \int_{-\frac{T}{2}}^{\frac{T}{2}} \sqrt{\Omega(t)^2 + \Delta(t)^2} dt + \frac{1}{2} [\phi(-\frac{T}{2}) + \phi(\frac{T}{2})], \quad (\text{S3})$$

where T is the pulse duration, $\Delta(t) = -\dot{\phi}(t)$ (assuming zero frequency detuning at the center of the ARP), $\phi(-\frac{T}{2})$ and $\phi(\frac{T}{2})$ denote the pulse phases at times $t = -\frac{T}{2}$ and $t = \frac{T}{2}$, respectively. Substituting the CHS pulse parameters into Eq. S3 yields the rotation-axis phase for the CHS pulse:

$$\phi_0^{\text{CHS}} = \frac{\pi}{2} - \frac{1}{2} \int_{-\frac{T}{2}}^{\frac{T}{2}} \sqrt{(\Omega_0 \operatorname{sech}(\beta t))^2 + (\mu \beta \tanh(\beta t))^2} dt - \mu \ln\left(\operatorname{sech}(\beta \frac{T}{2})\right) + \phi_0, \quad (\text{S4})$$

Thus, when all other CHS pulse parameters are held constant, the phase difference between CHS pulses depends solely on ϕ_0 , which aligns with the behavior of rectangular π -pulses.

For the CHS-UR4 sequence, setting $\phi_2 = \pi/2 + \delta$ results in the four pulse phases: 0, $\pi/2 + \delta$, 2δ , and $\pi/2 + 3\delta$, where δ ranges from 0 to 2π . Notably, the UR4 sequence reduces to the XY4 sequence when $\delta = 0$ [39]. The CHS-UR4 sequence features a linearly increasing phase $N \cdot \delta$, where N is the pulse index. Therefore, while the CHS-UR4 sequence uses a similar configuration as the XY4 sequence, it relaxes the requirement for strict $\pi/2$ phase shifts between adjacent pulses. Accordingly, by precisely controlling the time intervals between CHS pulses, which ensures the linearly increasing phase, and embedding the phase pattern [0, $\pi/2$, 0, $\pi/2$] within each CHS pulse waveform, the CHS-UR4 sequence can be accurately generated using standard arbitrary waveform generators (AWGs).

We employ an AWG (Zurich Instruments, HDAWG) to generate the CHS pulse waveforms. Given that the DD pulse intervals are on the order of seconds or even tens of seconds, the internal crystal-oscillator clock of the HDAWG cannot maintain sufficiently stable intervals (and the corresponding phase relationships) between CHS pulses. To ensure temporal stability across the DD sequence, we use a rubidium frequency standard as an external clock for the AWG. Each RF CHS pulse in our experiments has a duration of 3.9 ms, a bandwidth of 22 kHz, and a peak power of 150 W.

In summary, by combining the robustness of the UR4 sequence with that of individual CHS pulses, the CHS-UR4 DD sequence emerges as an excellent candidate for high-performance ensemble-based photonic quantum memories. For future work, efforts should focus on balancing the storage efficiency of the NLPE-DD memory at high pulse numbers against the accumulated population error induced by multiple pulses, thereby maximizing the achievable quantum memory lifetime.